Simulation of scanner- and patient-specific low-dose CT imaging from existing CT images

Naziroglu, Robiel; van Ravesteijn, Vincent; van Vliet, Lucas; Streekstra, G.J.; Vos, Frans

Important note
To cite this publication, please use the final published version (if applicable).
Please check the document version above.

Simulation of scanner- and patient-specific low-dose CT imaging from existing CT images

Robiël E. Naziroglu (1), Vincent F. van Ravesteijn (1), Lucas J. van Vliet (1), Geert J. Streekstra (2,3), Frans M. Vos (1,2)

1) Quantitative Imaging Group, Delft University of Technology, NL-2628 CJ Delft, The Netherlands. R.E.Naziroglu@tudelft.nl, L.J.vanVliet@tudelft.nl

2) Department of Radiology, Academic Medical Center, NL-1100 DD Amsterdam, The Netherlands, g.j.streekstra@amc.uva.nl

3) Department of Biomedical Engineering and Physics, Academic Medical Center, NL-1105 AZ Amsterdam, The Netherlands

Abstract

Purpose: Simulating low-dose Computed Tomography (CT) facilitates in-silico studies into the required dose for a diagnostic task. Conventionally, low-dose CT images are created by adding noise to the projection data. However, in practice the raw data is often simply not available. This paper presents a new method for simulating patient-specific, low-dose CT images without the need of the original projection data.

Methods: The low-dose CT simulation method included the following: (1) computation of a virtual sinogram from a high dose CT image through a radon transform; (2) simulation of a 'reduced'-dose sinogram with appropriate amounts of noise; (3) subtraction of the high-dose virtual sinogram from the reduced-dose sinogram; (4) reconstruction of a noise volume via filtered back-projection; (5) addition of the noise image to the original high-dose image. The required scanner-specific parameters, such as the apodization window, bowtie filter, the X-ray tube output parameter (reflecting the photon flux) and the detector read-out noise, were retrieved from calibration images of a water cylinder. The low-dose simulation method was evaluated by comparing the noise characteristics in simulated images with experimentally acquired data.

Results: The models used to recover the scanner-specific parameters fitted accurately to the calibration data, and the values of the parameters were comparable to values reported in literature. Finally, the simulated low-dose images accurately reproduced the noise characteristics in experimentally acquired low-dose-volumes.

Conclusion: The developed methods truthfully simulate low-dose CT imaging for a specific scanner and reconstruction using filtered backprojection. The scanner-specific parameters can be estimated from calibration data.

Keywords: Filtered Back Projection, Noise Power Spectrum, Bowtie Filter, Read-out Noise, Sinogram,

1 Introduction

Computed tomography (CT) has established itself as one of the most important medical imaging modalities [1]. In fact, the number of CT examinations is still increasing [2]. An important disadvantage of CT, however, is the exposure to ionizing radiation that is inherent to the technique

[1]. Accordingly, it is common practice to keep the radiation dose as low as reasonable achievable (ALARA). Unfortunately, lowering the dose yields a lower signal-to-noise ratio and thus a poorer image quality which may hamper subsequent diagnosis. Optimization of the dose/quality trade-off is a far from trivial problem as one cannot simply expose subjects to a range of radiation doses for ethical reasons. Alternatively, measurements on anthropomorphic phantoms allow real low dose measurements [3] [4]. However, such phantoms may not capture the large variability in structures that can be encountered in real life. Therefore, a lower-dose CT image is usually simulated by adding noise to the underlying projection data, i.e. the sinogram [5] [6] [7] [8] [9] [10] [11]. Subsequently, the lower-dose image is reconstructed from these noisy projections using the scanner's software. However, this approach is not always achievable in practice as the projection data are often simply not available. This paper studies a method to generate low-dose CT images based on existing image data. Therefore, we introduce new methodology to determine key system parameters such as the reconstruction kernel, bowtie filter, the X-ray tube output and the read-out noise by a simple calibration procedure. These system parameters determine the noise properties of the simulated low dose CT-images. Furthermore, retrospective investigation of the influence of low-dose imaging might be permitted if one could generate such data directly from existing images.

1.1 Related Work

Mayo et al [9] and Frush et al. [10] were among the first to simulate low-dose CT images. They added Gaussian noise to the projection data, after which the images were generated by means of the scanner's reconstruction software. Any such approach assumes that the number of photons hitting the detector is large. However, when only a low number of photons is detected, the properties of the noise in the sinograms become much more complex. Then, the readout noise becomes significant and the measured signal is best described by compound Poisson statistics [12] [13] [14]. Still, many low-dose CT-simulators have merely added Gaussian noise to the raw projection data [8] [15] [16] [7]. Zabic et al [17] extended the noise model to correctly reflect the noise (co)variances under photon-starvation conditions and appropriately simulate detector noise artifacts. Furthermore, Wang et al. combined the raw data acquired at two tube-voltages, which allowed also simulating adjustments in the tube-voltage [16]. Similarly, Wang et al [18] present a method for generating simulated low-dose cone-beam CT (CBCT) preview images. Essentially, correlated noise is injected into the original projections after which images are reconstructed using both conventional filtered backprojection (FBP) and an iterative, model-based image reconstruction method (MBIR).

Simultaneously, the need for meaningful characterization of image noise beyond that offered by pixel standard deviation became increasingly important [10] [8] [7] [19]. Boedeker et al. [20] and Faulkner et al. [21] proposed to use the NPS and the noise equivalent quanta (NEQ) to describe the noise properties in CT images, whereas Joemai et al. [7] used the NPS and variance to validate their low-dose CT model. Mieville et al. [22] investigated the spatial dependency and non-stationarity of the NPS. Verdun et al. [23] provide a review on image quality characterization and the dependency of the NPS and standard deviation on several scanner parameters.

The work that was done to describe the NPS of CT images also yielded techniques to estimate the reconstruction kernel. This proved very valuable information, since manufacturers are often reluctant to disclose the kernels. Other scanner-specific parameters, such as the bowtie filter and the readout noise, were derived from the projection data [8] [14] [12]. To the best of our knowledge the bow tie filter was never derived from actual image data.

In case projection data of the scanner is not available an approach based on simulated projection data from existing image reconstructions can be used to simulate low dose CT-scans. Initially, Wang

et al. [24] and Kim and Kim [25] presented preliminary work on simulating low-dose CT scans from the reconstructed images. Wang et al aimed to develop a simulation technique based on image data such that it produced similar results as a method using the original projection data. Kim and Kim [26] presented a comprehensive, image-based framework for reduced-dose CT simulation. The key characteristics of the CT system are estimated in this work based on several measurements of a tapered, cylindrical phantom: the reconstruction filter, noise parameters and the photon flux of the X-ray tube. Subsequently, reduced dose CT noise images are generated from a synthesized sinogram. The noise equivalent quanta (NEQ) is a key parameter that is used to determine the system parameters. Essentially, it reflects the (squared) SNR in a CT image, measured from the noise image of a uniform object. Kim and Kim adopt a linear relation between NEQ per detector element and the NEQ per image to specify the amount of noise that has to be added. This relation was derived (amongst others) by Wagner [27] and Hanson [28] assuming that the attenuation at the varying projection angles is uniform.

1.2 Objective

This paper presents a new framework to simulate lower-dose CT imaging from existing CT images without using the original projection data. We take a different approach to image-based low dose CT simulation compared to Kim et al [26]. The most important additional value compared to their work is that our approach enables estimation of all scanner-specific parameters directly from the calibration scans without requiring technical information provided by the manufacturer. In particular the estimation of the bowtie filter directly from the measurements is an important novelty of our work. Another difference is that our method for estimating the system parameters relies on the variance in signal intensity reflecting the noise level. While doing so we do not need to assume that the noise properties of the projections are uniform. Additionally, Kim used a small region of interest in the center (where the noise properties are uniform) of a tapered phantom to estimate the photon flux and the read-out noise. Instead, we can use the complete phantom to estimate the system parameters. As such, a larger region of the image is involved which should improve the precision of the estimation.

The paper is organized as follows. Section 2 describes the materials and methods; Section 2.1 descibes the CT-examinations, Section 2.2, the actual low-dose simulation method and Section 2.3 . Subsequently, Section 2.3 goes into how several system parameters can be estimated from CT images. The outcome is discussed in Section 4.

2 Material and methods

2.1 Materials

CT images of a water cylinder 34 cm in diameter and an anthropomorphic pelvic phantom were acquired on a Philips Brilliance 64 CT scanner at the Academic Medical Center in Amsterdam, The Netherlands. A modified CT colon protocol was used, since the intended application is CT colonography. The modifications only concerned the tube current, which was adjusted to control the dose level and the acquisition mode, which was sequential for the water cylinder (i.e. imaging the exact same plane) and the pelvic phantom. Table 1 list the parameter settings.

CT images of the water cylinder were used to estimate the unknown, scanner-specific parameters (see Section 2.3). Here, the settings listed under 'Calibration/Training' (Table 1) were used.

Subsequently, separate images of the water cylinder and images of the pelvic phantom were used to validate the low-dose simulation model (settings listed under 'Test'). Therefore, simulated and measured noise characteristics were compared by means of the pixel variances and the NPS.

Scan protocol parameters			
Phantom type	water cylinder		pelvic phantom
Acquisition mode	sequential		sequential
Kernel	B		B
X-ray tube Voltage (kV)	120		120
Slice Thickness	0.68		0.68
Collimation :w (mm)	40 x 0.625		64 x 0.625
Matrix	512 X 512		512 X 512
Diameter field of measurement: D_{FOM} (mm)	500		500
Set type	Calibration/ Training	Test	Test
Field of view	350	350	350
Pixel sizes: d_{pix}(mm)	0.68	0.68	0.68
Exposure: $I\tau$ (mAs)	250, 120, 60, 30	210, 170, 120, 85, 60, 42, 30, 20, 15	80, 40,15
Number of rotations	25 (except for 250 mAs: 100)	13	128
Copies per rotations	40	40	1
Number of slices	1000 (except for 250 mAs: 4000)	520	128

Table 1 Scan protocol parameters.

2.2 Lower-dose CT simulator

In our simulation method we first create a virtual sinogram from a high-dose CT image, which is processed to yield one corresponding to a lower dose. Subsequently, the high-dose virtual sinogram is subtracted from the lower-dose sinogram. The resulting noise sinogram is used to reconstruct a noise volume via filtered back-projection. Addition of the noise volume to the original high-dose image results in the lower-dose image.

Figure 1 presents an overview of the low-dose CT simulation steps,;

1. An attenuation image μ_{high} is constructed from a high-dose CT image J_{high};
2. A virtual sinogram R_{high} is generated from μ_{high} by means of the Radon transform [29] [30]. Note that computing the radon transform requires interpolation, hence this virtual sinogram is slightly more blurred than the true sinogram ;
3. A virtual, noiseless measurement of the number of detected photons $N_{\text{det, high}}$ is generated from R_{high};
4. A virtual, noisy measurement N_{red} at reduced dosed is created with appropriate amounts of Poisson and Gaussian noise — reflecting the quantum and readout noise components [1] as well as the noise already present in the original high-dose image;
5. A virtual, 'reduced'-dose sinogram R_{red} is computed from N_{red};
6. A noise sinogram R_{noise} is obtained by subtracting the virtual sinogram R_{high} from the reduced-dose sinogram R_{red}. This ensures that all smoothing effects that are inherent to the discrete radon transform (step 2) and the discrete inverse radon transform (step 7) do not impose additional blurring to the object being imaged;
7. A noise attenuation image μ_{noise} is reconstructed by means of the inverse Radon transform ---via filtered back-projection (FBP)--- from the noise sinogram R_{noise};
8. A noise image J_{noise} is constructed from μ_{noise};
9. A low-dose attenuation image J_{low} is formed by adding J_{noise} ---which contains noise only--- to the original high-dose CT image J_{high} (See Figure 2);

In the next subsections, we will detail steps 1—9; steps 1-3 in Section 2.2.1, steps 4-6 in Section 2.2.2.2 and steps 7-9 in Section 2.2.3

2.2.1 The virtual sinogram (Steps 1-3)

The attenuation image μ_{high} is calculated from the input, high-dose image J_{high} in step 1 via:

$$\mu_{\text{high}} = \frac{\mu_{\text{water}} J_{\text{high}}}{1000} + \mu_{\text{water}}, \tag{1}$$

in which we use for μ_{water} the attenuation coefficient of water at the effective energy of an X-ray tube of 80 keV [31] [32].

In step 2, the aggregate of such attenuation projections in a fan-beam scanner geometry $R_{\text{High}}(i,j)$ can be approximated from the high-dose attenuation image using the parallel-beam Radon transform followed by a reordering of the projections (Equation 130, page 93 [29]). Here, i represents a beam offset angle with respect to a gantry angle j. $R_{\text{High}}(i,j)$ should be considered an approximate, *virtual* sinogram, particularly since the noise is strongly reduced due to all the interpolations and averaging involved in its calculation. The associated, virtual transmission $T_{\text{high}}(i,j)$ and virtual noiseless measurement $N_{det,high}(i,j)$ are respectively calculated by:

$$T_{\text{high}}(i,j) = e^{-R_{\text{high}}(i,j)}, \tag{2}$$

and

$$N_{det,high}(i,j) = N_0(i) T(i,j), \tag{3}$$

in which $N_0(i)$ is the number of incident photons defined as;

$$N_0(i) = \frac{Kwd_{\text{fan}}I\tau}{M}T_B(i),\tag{4}$$

in which w is the collimation (width of the fan beam), d_{fan} the detector size in the fan angle direction at the isocenter, τ the rotation time, M the number of gantry angles per rotation, I the tube current, $T_B(i)$ the transmission of the bowtie filter and K a constant reflecting the X-ray tube output in photons/(mAs. mm^2). The parameters K and $T_B(i)$ are scanner-specific and need to be estimated using calibration scans (if not known a-priori), for which a procedure is detailed in Section 3.1. The other parameters in Eq. (4) can be typically retrieved from the literature [33] [1] or are included in the DICOM-header. Note that the radiation dose is steered via the exposure $I\tau$. Essentially, step 3 consists of calculating $N_{det,high}$ using Eqs. (2), (3) and (4).

2.2.2 Adding noise to the virtual sinogram

2.2.2.1 Background

This section describes the procedure to add an appropriate amount of noise to the virtual noiseless measurement in such a way that we account for the noise already present in the original image.

As such, the pixel variance of the low-dose image var[$\mu_{\text{low}}(n,m)$] is given by

$$\text{var}[\mu_{\text{low}}(n,m)] = \text{var}[\mu_{\text{high}}(n,m)] + \text{var}[\mu_{\text{noise}}(n,m)],\tag{5}$$

where var[$\mu_{\text{high}}(n,m)$] and var[$\mu_{\text{noise}}(n,m)$] are the pixel variances of the high-dose image and the noise image, respectively. As a result of filtered back-projection, *any* attenuation image $\mu(n,m)$ is a weighted sum of attenuation projections $R(i,j)$ and since the noise in the projections is assumed to be independent, the pixel variance equals

$$\text{var}[\mu(n,m)] = \left(\frac{\pi}{M}\right)^2 \sum_{j=1}^{M}\sum_{i=-N_{fan}}^{N_{fan}-1} c_{\text{tot}}(n,m,i,j)^2\,\text{var}[R(i,j)].\tag{6}$$

in which c_{tot} are the reconstruction filter coefficients incorporating all the filtering steps (e.g. necessary interpolation steps) and $2N_{fan}$ the number of detector elements. According to Eq. (6), the correct noise characteristics are created when each attenuation projection contains an appropriate amount of noise, hence the following condition should be satisfied:

$$\text{var}[R_{\text{low}}(i,j)] = \text{var}[R_{\text{high}}(i,j)] + \text{var}[R_{\text{noise}}(i,j)],\tag{7}$$

in which var[$R_{\text{high}}(i,j)$] is the variance in the high-dose sinogram, var[$R_{\text{low}}(i,j)$] the variance in a sinogram acquired at the specified dose and var[$R_{\text{noise}}(i,j)$] the variance in the zero-mean noise sinogram. $R_{noise}(i,j)$ is defined as

$$R_{\text{noise}}(i,j) = R_{\text{red}}(i,j) - R_{\text{high}}(i,j),\tag{8}$$

in which $R_{red}(i,j)$ is the reduced-dose sinogram with the noise characteristics so that Eqs. (7) is satisfied. Additionally, the variance of an attenuation projection var$[R(i,j)]$ can be approximated by a first order Taylor series approximation [34] [35] [14] as:

$$\text{var}[R(i,j)] \approx \frac{1}{N_{\text{det}}(i,j)} + \frac{\sigma_e^2}{N_{\text{det}}^2(i,j)}.\tag{9}$$

Eq. (9) consists of two terms. The first reflects the quantum (photon) noise, which obeys a Poisson distribution. The second term represents the readout noise, which is modeled by zero-mean

Gaussian noise $G(0, \sigma_e^2)$ with variance σ_e^2. Henceforth, the challenge is to simulate the reduced-dose measurement N_{red}, which consisted of adding two independent noise processes, namely quantum noise $N_{red,q}(i,j)$ and read-out noise $N_{red,r}(i,j)$,

$$N_{\mathrm{red}}(i,j) = N_{\mathrm{red,q}}(i,j) + N_{\mathrm{red,r}}(i,j).$$
(10)

2.2.2.2   Model Implementation (Steps 4-6)

First, only the quantum noise is simulated by drawing samples from a Poisson distributions with expectation value $N_{red,q}(i,j)$. $N_{red,q}(i,j)$ is calculated using Eqs. (3) and (4) at I_{red}, which is the tube current that yields the correct amount of noise to be used for creating the sinogram:

$$I_{\mathrm{red}} = \frac{I_{\mathrm{high}} I_{\mathrm{low}}}{I_{\mathrm{high}} - I_{\mathrm{low}}}$$
(11)

in which I_{high} and I_{low} are the tube currents of the high-dose and the low-dose image to be simulated. Eq. (11) is obtained after substituting Eqs. (3), (4) and the first term in the right hand side of Eq. (9) into Eq. (7) and reshuffling the terms. Note that this equation essentially compensates for quantum noise already present in the high-dose image.

Second, the readout noise is simulated by repeatedly drawing samples $N_{red,r}(i,j)$ from a Gaussian distribution with mean zero and variance σ_{red}^2. Given that $N_{red,r}$ is calculated as described previously, σ_{red}^2 is computed by substituting Eqs. (3), (4), (11) and the first term in the right hand side of Eq. (9) into Eq. (7), reshuffling the terms and dropping all redundant terms to yield:

$$\sigma_{\mathrm{red}}^2 = \sigma_e^2 \frac{I_{\mathrm{high}}^2 - I_{\mathrm{low}}^2}{\left(I_{\mathrm{high}} - I_{\mathrm{low}}\right)^2}.$$
(12)

As before, this equation compensates for Gaussian noise already present in the high-dose data. The virtual noisy measurement (step 4) is found by adding the read-out noise to the Poisson process as specified in Eq. (10). We adjust N_{red} and set it to one, whenever the equation delivers a number that is smaller than one (photon starvation), which corresponds to a very small $N_{red}(i,j)/N_0(i,j)$ as $N_0 >> 1$. Hence, the virtual 'reduced' dose sinogram (step 5) becomes

$$R_{\mathrm{red}}(i,j) = -\ln\left(N_{\mathrm{red}}(i,j)/N_0(i,j)\right),$$
(13)

the noise sinogram (step 6) is obtained using Eq. (8).

2.2.3   Reconstructing the image from the noisy sinogram (Steps 7-9)

In step 7, we opt to reconstruct $\mu(i,j)$ in a parallel-beam geometry , because it is computationally less expensive and because our scanner uses such a reconstruction approach [29]. Therefore, the fan-beam projections $R_{noise}(i,j)$ are first reordered into parallel-beam projections (Equation 130, page 93, [29]) Next, filtered back-projection is used to construct a noise image via:

$$\mu_{\mathrm{noise}}[n,m] = \left(\frac{\pi}{M}\right) \sum_{j=1}^{M_{par}} \sum_{i=-N_{fan}}^{N_{fan}-1} R_{\mathrm{noise}}(i,j) \cdot c_{tot}(n,m,i,j),$$
(14)

after which, $\mu_{\text{noise}}(n, m)$ was scaled to Hounsfield units in step 8 by:

$$J_{\text{noise}}(n,m) = 1000\left(\frac{\mu_{\text{noise}}(n,m) - \mu_{\text{water}}}{\mu_{\text{water}}}\right).$$ (15)

Finally, the low-dose image can be obtained in step 9 as:

$$J_{\text{low}}(n,m) = J_{\text{high}}(n,m) + J_{\text{noise}}(n,m).$$ (16)

2.3 Parameter estimation

This section describes how the required scanner- and scan-specific parameters may be computed from calibration scans:

1. The reconstruction filter coefficients in $c_{\text{tot}}(n, m, i, j)$
2. The bowtie filter transmission $T_B(i)$
3. The X-ray tube output parameter K
4. The readout noise variance σ_e^2

2.3.1 The reconstruction filter coefficients

Conventionally, the reconstruction filter $c_{\text{tot}}(n, m, i, j)$ is derived from the NPS in a region of interest (ROI) [26] [20] [21] [36]. If all fan-beam projections $R(i, j)$ used to reconstruct the ROI contain white noise (and aliasing is negligible), the NPS becomes radially symmetric [36]. This is approximately the case in the center of a water cylinder that is placed in the center of the scanner [22].

Therefore, the volumes emanating from successive X-ray tube rotations at 250 mAs were pairwise subtracted to yield 2000 zero-mean noise images (i.e. corresponding slices from successive rotations). As such the attenuation profile of water cylinder is implicitly corrected and any structured noise removed [20] [22]. The NPS was estimated in a small rectangular ROI consisting of 64x64 pixels in the center of the images through the periodogram, which is defined by,

$$\text{NPS}(\omega_x, \omega_y) = \sum_{i=1}^{N} \frac{|\text{F}\{J_{\text{noise}}(x,y)\}|^2}{N}$$ (17)

in which N is the number of images used to estimate the NPS, ω_x and ω_y are the frequencies in Cartesian coordinates and $\mathcal{F}\{\}$ symbolizes the Fourier transform. In such a ROI, the modulation transfer function of the scanner $H_{tot}(\omega_r)$ (e.i. $\mathcal{F}\{c_{\text{tot}}\}$) is related to the radially averaged NPS via:

$$\text{NPS}(\omega_r) = \frac{B_{const}}{\omega_r} H_{tot}^2(\omega_r),$$ (18)

where $\omega_r = \sqrt{\omega_x^2 + \omega_y^2}$, B_{const} is a scaling constant and division over ω_r depicts the density of the projections [37] [21]. In appendix C, we describe how to model H_{tot} and its parameters are determined by fitting the model to Eq. (18). Thereafter, $c_{tot}(l) = \mathcal{F}^{-1}\{H_{\text{tot}}(\omega_r)\}$

2.3.2 The bowtie filter

We will now demonstrate how the bowtie filter transmission can be estimated from the pixel variance measurements in a phantom.

Assuming that phantom images are acquired at a dose that is high enough to ignore the electronic noise, then the pixel variance var[$\mu(n, m)$] can be rewritten by substituting Eqs. (3) and (4) into Eq. (6):

$$\text{var}[\mu(n,m)] = \left(\frac{M^2 \pi^2}{I w d_{\text{fan}} K \tau} \right) \sum_{j=1}^{M} \sum_{i=-N_{fan}}^{N_{fan}-1} \frac{c_{\text{tot}}(n,m,i,j)^2}{T_B(i)T(i,j)}. \tag{19}$$

Apart from K and $T_B(i)$, the other parameters in this equation are known (c_{tot} may be estimated following the procedure from the previous section and $T(i,j)$ is obtained via Eq. (2)). Writing this equation in matrix notation yields:

$$\text{var}[\boldsymbol{\mu}] = A\mathbf{W}\mathbf{T_B}^{-1}, \tag{20}$$

where var[$\boldsymbol{\mu}$] is an N_{pix} vector (with N_{pix} again the number of pixels); $A = \frac{M^2\pi^2}{Iwd_{fan}K\tau}$ is a scalar; $\mathbf{T}_B$ is an $2N_{fan}$ vector representing the bowtie filter transmission and $\mathbf{W}$ is an $N_{pix} \times 2N$ matrix with elements w_{ki} ;

$$w_{ki} = \sum_{j=1}^{M} \frac{c_{\text{tot}}(n_k, m_k, i, j)^2}{T(i,j)} \tag{21}$$

Clearly, Eq. (20) is a linear equation that might be solved analytically. Unfortunately, the system matrix and the number of parameters are very large, and therefore such a purely analytic approach is computationally very expensive. Therefore, we opt to model the bowtie filter's transmission by:

$$T_B(i) = o_{\text{low}} + (1 - o_{\text{low}})\left(\sum_{q=0}^{4} a_q \cos\left(\frac{\pi q i}{N} \right) \right)^2. \tag{22}$$

The summation in the equation represents a truncated fourth order Fourier series. Only cosines are used as the bowtie filter is a symmetric function and the sum is squared to ensure that the transmission is not negative. Furthermore, we assume that the transmission in the center of the bowtie filter is one ($T_B(0) = 1$), which is imposed by constraining $a_0 = 1 - \sum_{q=1}^{4} a_q$. Furthermore, o_{low} is a constant representing the minimal transmission.

We assert that T_B is a monotonically decreasing function to both sides of the filter. Therefore, we devised the following simple penalty term:

$$P(\mathbf{a}) = \sum_{i=0}^{N-1} \frac{\partial T_B(i,\mathbf{a})}{\partial i} u\left(\frac{\partial T_B(i,\mathbf{a})}{\partial i} \right), \tag{23}$$

with $u(\cdot)$ the Heavyside function and $\mathbf{a}$ the 4 parameter vector of the model (c.f. Eq. (22)). Essentially, Eq. (23) sums all positive derivative values over half the filter (which is symmetric by definition).

Finally, the filter parameters are estimated by solving:

$$\mathbf{a}, \mathbf{A} = \arg\min_{\mathbf{a},\mathbf{A}} \left\{ \sum_{k=1}^{N_{\text{pix}}} \chi_k(\mathbf{a}, \mathbf{A}, k) + \beta P(\mathbf{a}) \right\}, \tag{24}$$

with

$$\chi_k(\mathbf{a}, \mathbf{A}, k) = \left(\text{var}[\mu_k]_{\text{experimental}} - \text{var}[\mu_k, \mathbf{a}, \mathbf{A}]_{\text{model}} \right)^2, \tag{25}$$

where A is the scaling constant from Eq. (20) which is essentially a gain factor that needs to be simultaneously estimated and β the weight of the penalty term

The required pixel variances to solve this equation are obtained from 4000 pairwise subtracted images of a water cylinder at 250mAs (see Table 1 and Figure 3). Subsequently, samples were collected from within the remaining region along 80 evenly distributed radial lines drawn outward from the center (see Figure 3). The bowtie filter parameters $\mathbf{a}$ were estimated for each of the 80 radial segments separately (via Eq. (24)), after which the associated bowtie filter transmissions were averaged. The initial parameter setting for every estimation was $\mathbf{a}_{init}$ = 0.5, 0, 0, 0, which corresponds to a single cosine (see below). o_{low} was set to 0.15, which is comparable to the minimum found in other scanners [12] [8].

2.3.3 The X-ray tube output parameter and the readout noise level

Finally, we will demonstrate how the X-ray tube output parameter K and the variance of the readout noise σ_e^2 can be estimated from the pixel variance $\text{var}[\mu(n, m)]$ measured at different tube currents. Therefore, Eq. (6) will be simplified in such a way that K and σ_e^2 can be derived from a linear fit.

First, substituting Eq. (9) into Eq. (6) yields:

$$\text{var}[\mu(n,m)] = \left(\frac{\pi}{M} \right)^2 \sum_{j=1}^{M} \sum_{i=-N}^{N-1} c_{\text{tot}}(n,m,i,j)^2 \left(\frac{1}{N_{\text{det}}(i,j)} + \frac{\sigma_e^2}{N_{\text{det}}(i,j)^2} \right) \tag{26}$$

Subsequently, substituting Eqs. (3) and (4) into (26) and reshuffling the variables yields

$$\text{var}[\mu(n,m)] = \left(\frac{\pi^2}{IM^2 wK\tau} \right) \sum_{j=1}^{M} \sum_{i=-N}^{N-1} \frac{c_{\text{tot}}(n,m,i,j)^2}{T_B(i)T(i,j)} + \left(\frac{\pi\sigma_e}{IKMw\tau} \right)^2 \sum_{j=1}^{M} \sum_{i=-N}^{N-1} \frac{c_{\text{tot}}(n,m,i,j)^2}{T_B(i)^2 T(i,j)^2}. \tag{27}$$

Consequently, the next relation emerges when the exposure $I\tau$, the X-ray tube output K, and the variance of the readout noise σ_e^2 are separated from all other variables of Eq. (27):

$$\text{var}[\mu(n,m)] = \frac{C_p(n,m)}{KI\tau} + \frac{C_e(n,m)}{K^2 I^2 \tau^2} \sigma_e^2, \tag{28}$$

in which $C_p(n, m)$ and $C_e(n, m)$ are given by

$$C_p(n,m) = \left(\frac{\pi^2}{M^2 w} \right) \sum_{j=1}^{M} \sum_{i=-N}^{N-1} \frac{c_{\text{tot}}(n,m,i,j)^2}{T_B(i)T(i,j)}, \tag{29}$$

and

$$C_e(n,m) = \left(\frac{\pi^2}{w^2 M^2}\right) \sum_{j=1}^{M} \sum_{i=-N}^{N-1} \frac{c_{\text{tot}}(n,m,i,j)^2}{T_B(i)^2 T(i,j)^2}. \tag{30}$$

$C_p(n,m)$ and $C_e(n,m)$ can be calculated using the reconstruction filter weights c_{tot} (from Section 2.3.1), the bowtie filter (from Section 2.3.2), and the transmission (calculated via Eq. (2)). Eq. (28) is ill-posed whenever the variance is measured at a single exposure. Therefore, acquisitions are obtained at multiple exposures. Next, the model is fitted in a least-squares sense using the following non-linear model,

$$\{K, \sigma_e^2\} = \arg\min_{K,\sigma_e^2} \left\{ \sum_{k=1}^{N_{\text{pix}}} \sum_{i=1}^{N_I} \chi_{k,i}(K, \sigma_e^2) \right\}, \tag{31}$$

with

$$\chi_{k,i}(K, \sigma_e^2) = \left(\text{var}[\mu_{k,i}]_{\text{measured}} - \text{var}\left[\mu_{k,i} \mid K, \sigma_e^2\right]_{\text{model}} \right)^2, \tag{32}$$

in which the model is expressed by Eq. (28), N_{pix} and N_I define the number of pixels and exposures respectively. The variance per pixel was estimated from the water cylinder images for each exposure level in the training set. The initial parameters are obtained by first solving a simpler problem that emerges when Eq. (28) is approximated by two linear equations. If the tube current is very high, the contribution of the read-out noise to the pixel variance is often neglected. In this case, the second term in the right hand side of Eq. (28) is ignored, hence K can be approximated from :

$$\text{var}[\mu(n,m)] \approx \frac{C_p(n,m)}{I\tau K}. \tag{33}$$

With K known, σ_e^2 can be estimated using new images that are acquired at a lower dose level. Reshuffling Eq. (28) gives:

$$\sigma_e^2 = \frac{K^2 \tau^2 I^2}{C_e(n,m)} \left(\text{var}[\mu(n,.m)] - \frac{C_p(n,m)}{KI\tau} \right). \tag{34}$$

These estimates for K and σ_e^2 are the initial parameters for minimizing Eq. (31).

3 Results

3.1 Parameter estimation

3.1.1 The reconstruction filter coefficients

Figure 4 shows the estimated 2D-NPS. Subsequently, the parameters of the apodization window H_{apo} were estimated by fitting our model (Appendix C) to the NPS. The left plot of Figure 5 demonstrates how well the model fits the data, while the right plot shows in blue the apodization window which is

used in the remainder of the paper (Eq. (37)). In the same plot, the algorithmic transfer function, H_{alg},

which is defined by $H_{alg}(\omega) = \left(\dfrac{H_{tot}(\omega_r)}{\omega_r} \right)$ and represents the total apodization, is depicted in pink.

3.1.2   The bowtie filter

Figure 6 shows the estimated bowtie transmission. The left plot gives the profile of the mean bowtie transmission, its 95% confidence interval (all in blue) as well as the initialization (pink). Notice that the bowtie transmission was estimated more precisely for the central detectors than for the ones at the periphery (reflected in the smaller confidence interval). Particularly, the variance is large for the range of |DetectorID| > 200, which corresponds to the edges of the water cylinder.

The right plot displays the variance measured (blue) along one of the radial segments depicted in Figure 3. Additionally, the variance as a function of position was computed by means of Eq. (20) with (pink) and without the bowtie filter (green). This shows that adding the bowtie filter to the model, enabled it to describe the measured variance more accurately.

The shape of the transmission profile was similar to previously estimated bowtie filters of CT-scanners [8] [12].

3.1.3   The X-ray tube output parameter and the readout noise level

Table 2 lists the estimated values of K and σ_e^2 at each exposure level. K was estimated using Eq. (33) by fitting a line through all data points, after which the slope of the line corresponds to $1/(I\tau K)$. Clearly, the estimation of K stabilizes at higher exposure levels and increasingly deviates from stability as the exposure level decreases. We attribute this to the increasing importance of the read-out noise due to which Eq. (33) is not valid anymore. Henceforth, the estimated value for K at 250 mAs is used as an initialization to compute the initial value of σ_e^2. The weighted average of estimates of σ_e^2 over all exposure levels is used to initialize the minimization procedure described by Eq. (31). Here, the weights were inversely proportional to the variances in the estimations of σ_e^2.

Exposure (mAs)	250	120	60	30
$K(\ \times\ 10^6)$	2.08 ± 0.38	2.03 ± 0.37	1.98 ± 0.35	1.84 ± 0.35
$\sigma_e{}^2$	-1 ± 85	11 ± 40	11.8 ± 20	15 ± 11

Table 2 Estimates for K and $\sigma_e{}^2$ at each exposure level. $\sigma_e{}^2$ is computed using K estimated at 250 mAs. K is expressed in the number of photons∕(mm². mAs.revolution).

The final values of K and σ_e^2 were estimated using Eq. (31) Eq. (32) and the weighted mean of the values in Table 2 as an initialization. They were found to be $2.17*10^6$ photons∕(mm². mAs) and 23.3(average of the values at the lowest two exposures), respectively. Note that K and σ_e^2 are higher

as all data were combined than for each tube current separately. These final values will be used in the remaining experiments.

3.2 Validation of the low-dose CT model

The noise characteristics from simulated low-dose CT images were compared with those produced by experimental low-dose CT-scans to validate our method. The scan parameters to do so are collated in Table 1 (The 'Test' column under 'water cylinder' and under 'pelvic phantom'). The highest exposure level given in the table served as input to simulate low-dose images. The noise characteristics of all generated low-dose CT images were assessed by means of the pixel variance describing the noise 'strength', and the NPS quantifying the noise structure. Both were computed in a number of ROIs.

3.2.1 Water cylinder phantom measurements

Figure 7 shows a CT image indicating the positions of the ROIs that were used to compute the NPS. Each ROI had a size of 64x64 pixels.

Furthermore, Figure 8 shows the standard deviation as a function of the distance to the center at different exposure levels: 60 mAs (lower three) and 15 mAs (upper three), respectively. The simulations at 60mAs (bottom three curves) were obtained using images scanned at 250mAs (bottom), 120mAs (middle) and 85mAs (top), while the simulations at 15mAs (top three curves) used images obtained at 250mAs (bottom), 60mAs (middle) and 21mAs (top). The pink and blue lines correspond to the angular averaged experimental and the simulated data.

Figure 8 shows that the differences between simulations and experiments are small. Only in the centre of the 15 mAs simulations small differences of maximally 5% are noticeable. Notice that the (small) deviation becomes larger in simulations from increasingly higher doses. This is because increasingly more noise is added, yielding larger fluctuations in the simulations.

Figure 9 shows contour plots of the NPS calculated from ROIs depicted in Figure 7. The blue and pink lines correspond to the experimental and the simulated NPS, respectively. The shape of the 2D noise power spectra from the simulations closely approximates those encountered experimentally.

A global comparison of the noise in the simulations and the experimental data is contained in the supplementary material.

3.2.2 Pelvic phantom

Fifteen ROIs were selected in which the noise properties were analyzed, see Figure 10. Each ROI was composed of 41 x 41 pixels. The standard deviation in each ROI was determined for both the experimental scans and the simulated scans at 80, 40 and 15 mAs. For the simulations at 40 and

15 mAs, the scans at 80 mAs were used as the high-dose image. A validation at 80 mAs was possible by computing the noise properties directly from the zero-mean noise image μ_{noise} that was simulated assuming the original image was acquired at infinite dose. For each slice and exposure level, 64 simulations were created to take variations in noise realizations into account. On average, the standard deviation of the simulated images deviated 5.3%, 2.4% and 4.3% from the standard deviation of the experimental images for the experimental acquired scans at 80, 40 and 15 mAs, which was within the 95% confidence interval of the estimated standard deviation.

Exposure (mAs)	slope	offset	correlation
80	0.995	1.71	0.994
40	1.006	0.94	0.998
15	1.018	1.75	0.994

Table 3 The parameters and the correlation of the linear fit illustrated in Figure 11

Figure 11 and Table 3 show that the simulated scans closely approximated the noise strength in the experimental scans. Nonetheless, the difference between the simulations and experimental scans was larger for the measurements based on the pelvic phantom than the ones based on the water cylinder. We attributed this to the presence of bone-like structures, that cause beam hardening ,which was not taken into account in our method.

Furthermore, the NPS was computed in four arbitrarily selected ROIs from experimental and simulated scans at 15 mAs, see Figure 12. Once more, the figures show how well the simulation technique approximates the experimentally acquired low-dose images.

A global comparison of the noise in the simulations and the experimental data of the pelvic phantom is contained in the supplementary material, just like the water cylinder phantom.

4 Discussion

We presented a novel method to simulate patient-specific, low-dose CT images from existing high-dose images assuming reconstruction by parallel beam filtered backprojection. Scanner-specific parameters i.e. the apodization window of the reconstruction filter, the bowtie filter, the X-ray tube output parameter and the read-out noise were estimated using calibration images of a water cylinder. Therefore, new estimators were developed that used reconstructed images and did not require projection data. The low-dose simulation was evaluated by comparing the noise characteristics of simulated low-dose images with experimentally acquired low-dose images.

One of the main strengths of our paper is that it allows scientists to simulate low-dose CT in a well-documented and reproducible manner while not being dependent on the availability of raw projections as well as scanner- and scanning-parameters. Note that it is not our purpose to improve

on the simulation methods that are based on the raw-projection data. Instead, the aim is to simulate low dose CT image from the higher dose images, which is useful whenever the raw projection data is not shared by vendors. Additionally, it is relevant for retrospective CT-studies in which the raw data is usually not stored. Moreover, it is important for the developers of image processing algorithms: it gives them a realistic tool to study the robustness of their techniques under noisy circumstances.

We demonstrated that the models used to recover the scanner-specific parameters accurately described the calibration data. The estimated reconstruction filter corresponded well to smooth reconstruction kernels found earlier [20] [25] [26]. We recognize, however, that a more general model such as an higher order cosine series may be necessary to describe the very sharp kernels. The shape of the bowtie filter estimated by us closely resembles the bowtie filter used in a Siemens scanner [12] [8] [38]. Furthermore, we estimated the X-ray tube output parameter at $K = 2.17*10^6$ photons$/$mm^2. mAs and the read-out noise variance at $\sigma_e^2 = 23.2$. These estimated values were of the same order of magnitude as reported previously: Massoumzadeh et al. [8] estimated $2.7*10^6$ photons$/$mm^2.mAs for K and values from 40 through 200 for σ_e^2; Faulkner et al. [21] estimated $4.15*10^6$ and $6.46*10^6$ photons$/$mm^2.mAs for K. Ma et al. [14] found 10 for σ_e^2. Finally, we showed that the simulated low-dose images accurately reproduced the noise in experimental low-dose volumes.

A limitation of our approach is in the assumption that monochromatic photons are produced by a virtual X-ray source. As such, our method does not take beam hardening effects into account, which likely cause the encountered deviations in the noise characteristics between simulated and experimental scans of the pelvic phantom. At the same time, the differences between the simulated and experimental data were relatively small even in the presence of bony structures and at relatively low exposures of 15 mAs. Essentially, a polychromatic approach would require a spectral dependency in our framework, particularly concerning the x-ray tube output N_0 and the calculation of attenuation projections. We consider this an important topic for further research. A study involving different scanners .is another, obvious topic for future work.

A limitation is that our method does not take tube current modulation into account. The tube current modulation essentially adjusts the tube current to the part of the body being imaged and the size of the patient [39]. A variation per slice can be simply incorporated in our method by adjusting N_0 to the actually used tube current I_{high} which may be stored in the DICOM-header. However, it might not be easy to recover complex variations of N_0, e.g. as a function of the gantry angle.

Our method requires a full field of view which is the case for many protocols. Clearly, one could always prospectively reconstruct full field images to satisfy this requirement. In our model, the detector noise was approximated by zero-mean Gaussian noise, which is commonly used in literature [25] [14] [8] [40] [24], but strictly speaking is not entirely correct [17].

The techniques to extract the system parameters assumed in-plane, fan beam imaging and filtered backprojection for tomographic reconstruction. This should be considered a calibration step. The simulation method also focused on in-plane fan-beam imaging and image reconstruction by filtered backprojection, particularly to demonstrate the feasibility of simulating low dose CT scanning from higher dose images. As such, the effects of interslice noise correlations associated with helical scanning were not considered. We hypothesize that these correlations are small, but might not be negligible. An obvious next step will be to simulate cone-beam imaging and backprojection and fully integrate helical scanning in the model. This would require a fairly straightforward adaptation of the methods to generate the virtual sinogram and the technique to perform filtered backprojection.

Our methods are not applicable to iterative reconstruction methods as such methods violate crucial model assumptions (e.g. the pixel noise is not a weighted sum of the projection data). Clearly, system parameters may always be estimated with our methods based on images reconstructed with filtered backprojection. However, simulating low dose-CT images from iterative algorithms requires a method that can predict how the noise properties of such images evolve while the tube current is lowered. This remains far from trivial, due to all the nonlinear steps of the reconstruction procedures. This is perhaps the largest limitation of our work. Simultaneously, one could argue that as long as filtered backprojection is offered on scanners, its image quality could serve as a reference standard for iterative method. The proposed method is a valuable tool in this perspective.

4.1 Conclusion

The developed methods truthfully simulated low-dose CT imaging without requiring projection data. Moreover, all scanner-specific parameters were estimated directly from the calibration scans of a single phantom without requiring technical information provided by the manufacturer. This new technology might facilitate large-scale studies into the diagnostic accuracy for lower CT dose. In turn, it could aid in further reducing the radiation risks of CT-examinations.

Acknowledgments

References

[1]   Kalender WA. Computed Tomography. Publicis MCD Verlag; 2000.

[2]   OECD. Computed tomography CT exams (indicator) [Internet]. 2016.

[3]   Gabusi M, Riccardi L, Aliberti C, Vio S, Paiusco M. Radiation dose in chest CT: Assessment of size-

specific dose estimates based on water-equivalent correction. Physica Medica. 2016;32:393-397.

[4] Brix G, Lechel U, Sudarski S, Trumm C, Henzler T. Spectral optimization of iodine-enhanced CT: Quantifying the effect of the tube voltage on image quality and rdiation exposure determined at anthropomorphic phantom. Physica MEdica. 2016;32:999-1006.

[5] Florie J, Gelder RE, Schutter MP, van Randen A, Venema HW, de Jager S, van der Hulst VPM, Prent A, Bipat S, Bossuyt PMM, et al. Feasibiliy study of computed tomography colonography using limited bowel preparation at normal and low-dose levels study. Eur. Radiol. 2007;17(12):3112-22.

[6] Gelder RE, Venema HW, Florie J, Nio CY, Serlie IWO, Schutter MP, van Rijn JC, Vos FM, Glas AS, Bossuyt PMM, et al. CT colonography: Feasibility of Substantial Dose Reduction -- Comparison of Medium to Very Low Doses in Identical Patients. Radiology. 2004;232(2):611-20.

[7] Joemai RMS, Geleijns J, Veldkamp WJH. Development and validation of a low dose simulator for computed tomography. Eur. Radiol. 2010;20(4):958-66.

[8] Massoumzadeh P, Don S, Hildebolt CF, Bae KT, Whiting BR. Validation CT dose-reduction simulation. Medical Physics. 2009;36:174-189.

[9] Mayo JR, Whittal KP, Leung AN, Hartman TE, Park CS, Primack SL, Chambers GK, Limkeman MK, Toth TL, Fox SH. Simulated dose reduction in conventional chest CT: validation study. Radiology. 1997 453-457.

[10] Frush DP, Slack CC, Hollingsworth CL, Bisset GS, Donnelly LF, Hsieh J, Lavin-Wensell T, Mayo JR. Computer-simulated radiation dose reduction for abdominal multidetector CT of pediatric patients. Am. J. Roentgenol. 2002;179(5):1107-13.

[11] Amir O, Brunstein D, Altman A. Dose optimization tool. In: Medical Imaging 2003: Visualization, Image-Guided Procedures and Display; 2003. p. 815-821.

[12] Whiting BR, Massoumzadeh P, Earl OA, O'Sullivan JA, Snyder DL, Williamson JF. Properties of preprocessed sinogram data in X-ray computed tomography. Med. Phys. 2006;33(9):3290-303.

[13] Yang K, Kwan ALC, Huang SY, Packard NJ, Boone JM. Noise power properties of a cone-beam CT system for breast cancer detection. Med. Phys. 2008;35(12):5317-27.

[14] Ma J, Liang Z, Fan Y, Liu Y, Huang J, Chen W, Lu H. Variance analysis of X-ray CT sinograms in the presence of electronic noise background. Med. Phys. 2012;39(7):4051-65.

[15] Wang AS, Pelc NJ. Synthetic CT: Simulating low dose single and dual energy protocols from a dual energy scan. Med. Phy. 2011;38:5551-5562.

[16] Wang AS, Pelc NJ. Synthetic CT: simulating arbitrary low dose single and dual energy protocols. In: Medical Imaging 2011: Physics of Medical Imaging, Poc. SPIE 7961; 2011.

[17] Zabic S, Wang Q, Morton T, Brown KM. A low dose simulation tool for CT systems with energy integrating detectors. Med. Phys. 2013 031102.

[18] Wang AS, Webster Stayman J, Otake Y, Vohgt S, Kleinszig G, Jay Khanna A, Gallia GL, Siewerdsen

JH. Low-dose preview for patient-specific, task-specific technique selection in cone-beam CT. Medical Physics. 2014;41(7):071915.

[19] Britten AJ, Crotty M, Kiremidjian A, Grundy H, Adam EJ. The addition of computer simulated noise to investigate radiation dose and image quality in images with spatial correlation of statistical noise: an example application to X-ray CT of the brain. Br. J. Radiol. 2004;77(916):323-8.

[20] Boedeker KL, Cooper VN, McNitt-Gray MF. Application of the noise power spectrum in modern diagnostic MDCT: part I. Measurement of noise power spectra and noise equivalent quanta. Phys. Med. Biol. 2007;52(14):4027-46.

[21] Faulkner K, Moores BM. Analysis of X-ray computed tomography images using the noise power spectrum and autocorrelation function. Phys. Med. Biol. 1984;29(11):1343-52.

[22] Mieville FA, Bolard G, Bulling S, Gudinchet F, Bochud FO, Verdun FR. Effects of computing parameters and measurement locations on the estimation of 3D NPS in non-stationary MDCT images. Physica Medica. 2013;29:684-694.

[23] Verdun FR, Racine D, Ott JG, Tapiovaara MJ, Toroi P, Bochud FO, Veldkamp WJH, Schegerer A, Bouwman RW, Hernandez Giron I, et al. Image quality in CT: From physical measurements to model observers. Physica Medica. 2015;31:823-843.

[24] Wang AS, Feng S, Pelc NJ. Image-based synthetic CT: simulating arbitrary low dose single and dual energy protocols from dual energy images. In: Medical Imaging 2012: Physics of Medical Imaging, Proc. SPIE 8313; 2012.

[25] Kim CW, Kim JH. Application of CT Simulation Technique for Virtual Ultra-Low-Dose Trial in CT Colonography. In: Abdominal Imaging, Computational and Clinical Applications, 4th International Workshop; 2012; Nice, France. p. 49-57.

[26] Kim CW, Kim JH. Realistic simulation of reduced-dose CT with noise modeling and sinogram synthesis. Med. Phys. 2014;41(1):011901.

[27] Wagner RF, Brown DG, Pastel MS. Application of information theory to the assessment of computed tomography. Med. Phys. 1979;6(2):83-94.

[28] Hanson KM. Detectability in computed tomographic images. Med. Phys. 1979;6(5):441-451.

[29] Kak AC, Stanley M. Principles of Computerized Tomographic Imaging. IEEE Press; 1988.

[30] Prince JL, Links JM. Medical Imaging Systems. Pearson Prentice Hall; 2006.

[31] Hubbel JH, Seltzer SM. Tables of X-Ray Mass Attenuation Coefficients and Mass Energy-Absorption Coefficients (version 1.4). [Internet]. 2004 Available from: http://physics.nist.gov/xaamdi , [Accessed: 2017, February 8].

[32] Wunderlich A, Noo F. Image covariance and lesion detectability in direct fan-beam X-ray computed tomography. Phys. Med. Biol. 2008;53(10):2471-93.

[33] ImPACTGroup. Comparitive specifications: 64-slice CT-scanners. Centre for Evidence-based

Purchasing; 2009. CEP08027.

[34] Papoulis A. Probability, random variables and stochastic processes. McGraw-Hill; 1984.

[35] Macoviski A. Medical Imaging Systems. Prentice-Hall; 1982.

[36] Kijewski MF, Judy PF. The noise power spectrum of CT-images. Phys. Med. Biol. 1987;32(5):565-75.

[37] Riederer SJ, Pelc NJ, Chesler DA. The noise power spectrum in computed X-ray Tomography. Phys. Med. Biol. 1978;23(3):446-54.

[38] Wang J, Lu H, Liang Z, Eremina D, Zhang G, Wang S, Chen J, Manzione J. An experimental study on the noise properties of X-ray CT sinogram data in Radon space. Phys. Med. Biol. 2008;53(12):3327-41.

[39] Soderberg M, Gunnarsson M. Automatic exposure control in computed tomography -- an evaluation of systems from different manufacturers. Acta Radiol. 2010;51(5):625-34.

[40] Benson TM, de Man BKB. Synthetic CT noise emulation in the raw data domain. In: IEEE Nuclear Science Symposuim & Medical Imaging Conference; 2010. p. 3169-3171.

Captions
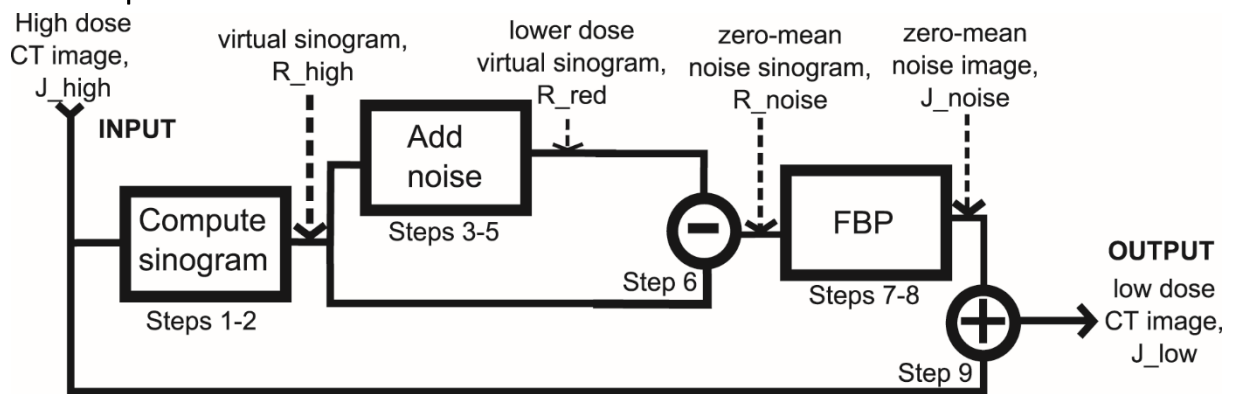
Figure 1: Schematic overview of the low-dose CT simulator

| high dose | noise | low dose |
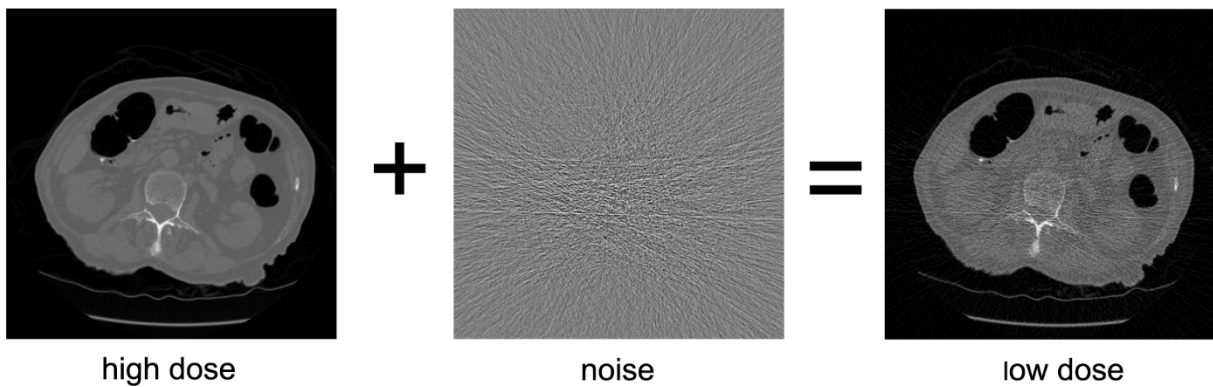
Figure 2: A low-dose CT image J_{low} (right) is simulated by adding a patient-specific (zero-mean) noise image J_{noise} (middle) to the original high-dose image J_{high} (left).
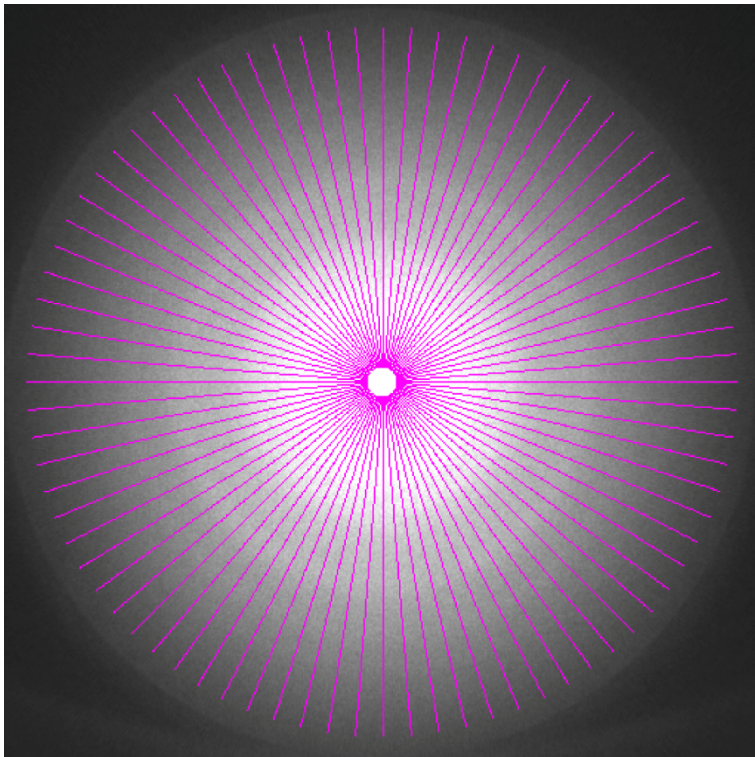
Figure 3: Variance image and all of the radial segments. The bowtie filter was calculated for each such segment, i.e. for each separate line on either side of the center.
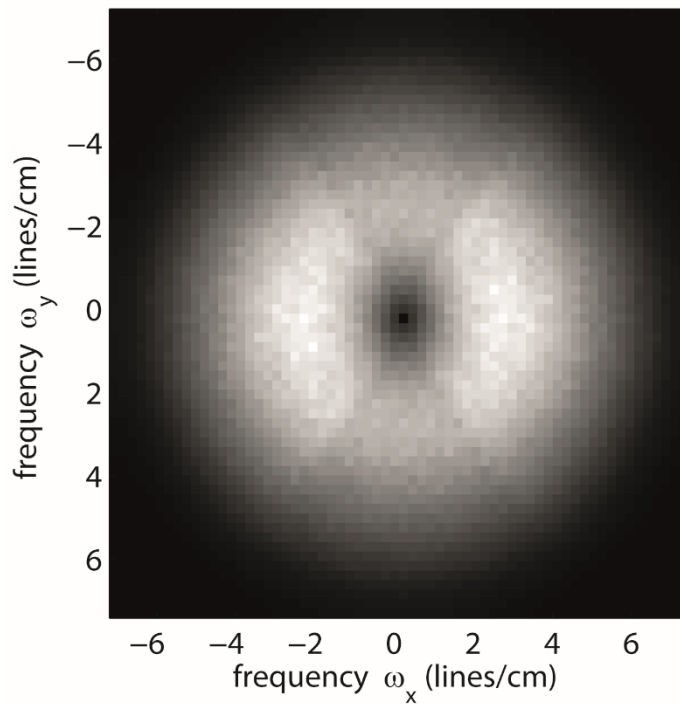

Figure 4: The NPS calculated from a 64x64 ROI in the center of a 34cm water cylinder. The NPS was normalized such that it ranged from 0 to 1
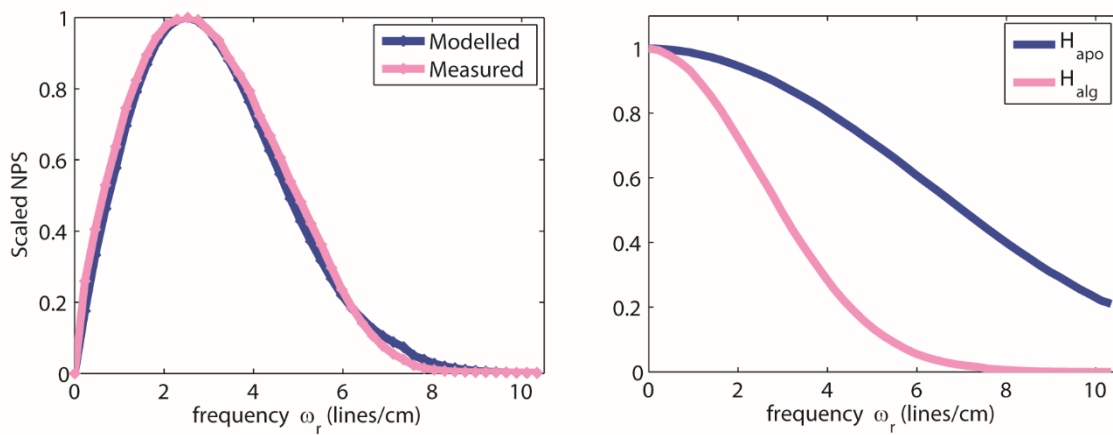
Figure 5: Left: the (angular averaged) radial NPS calculated from the images of a water cylinder (pink) and the fitted model, i.e. Eq. (38) (blue). Right: the ensuing apodization window H_{apo} (blue, Eq. (37)) and the algorithmic transfer function, H_{alg}.
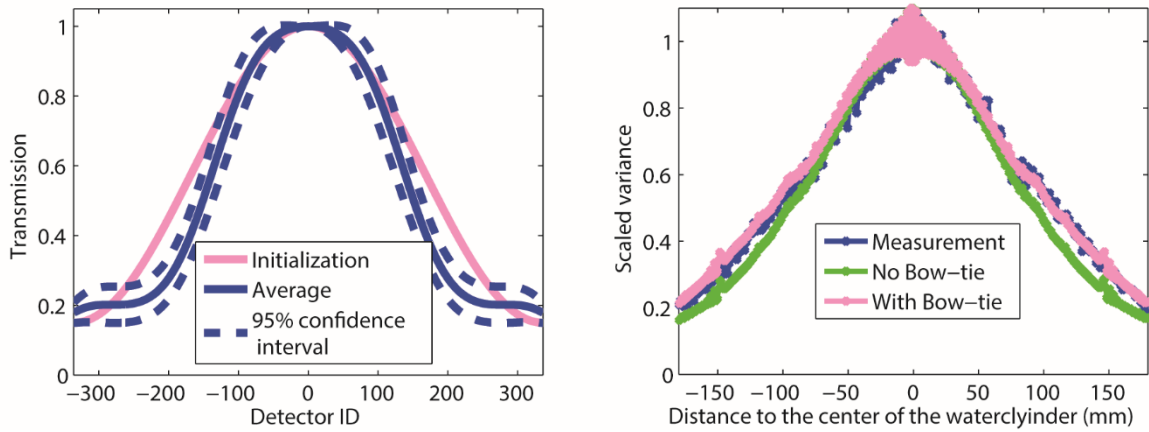
Figure 6: left: The mean estimated bowtie filter (blue solid), the 95% confidence intervals(blue dashed) and the bowtie used as initialization (pink). right: the values of the pixels measured (blue) on the diagonal of the variance image depicted in Figure 3, the analytically computed variance with (pink) and without (green) bowtie filter. The variance was scaled by dividing the original by the mean.
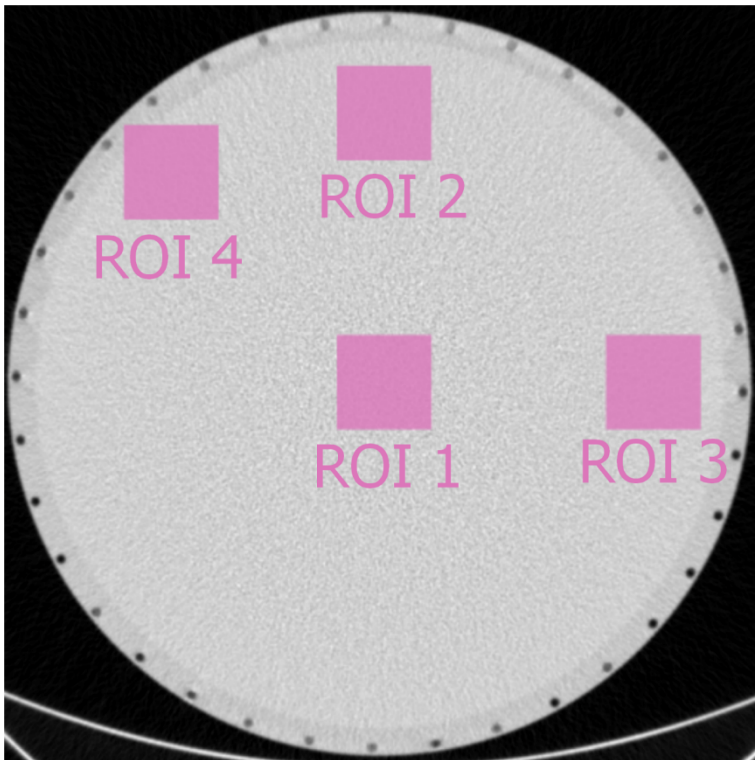

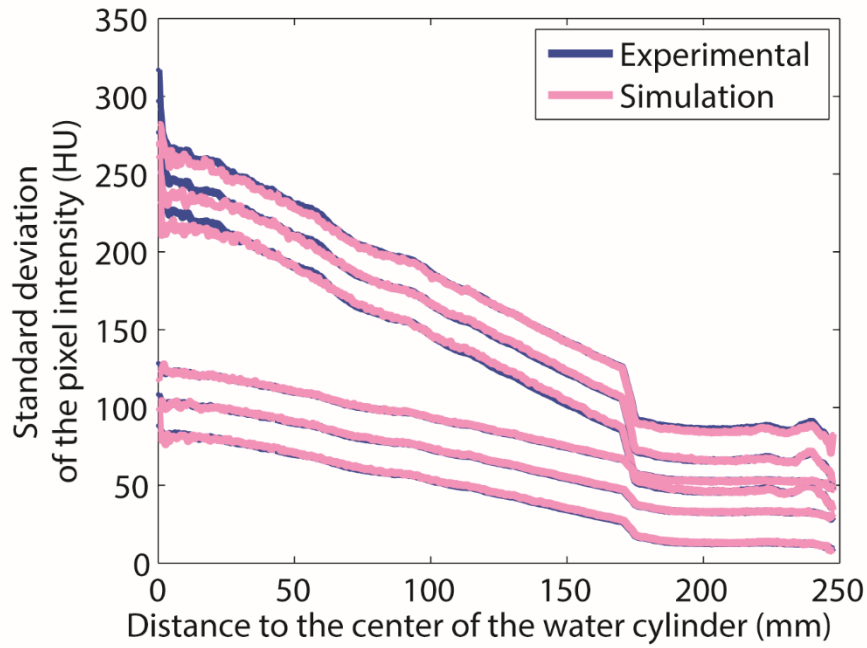Figure 7: Image depicting four ROIs that were used to validate the low-dose CT simulation.

Figure 8: The standard deviation of the noise in a 34cm water cylinder as a function of the distance to the center of the water cylinder for simulations of 15mAs data (top three lines) from images obtained at (from top to bottom) 21, 60 and 250 mAs and for simulations of 60mAs data from images obtained at (from top to bottom) 85, 120 and 250 mAs. An offset of -+20HU was added to separate the three curves for display purposes. The pink lines resulted from experiments, the blue lines from our simulations.
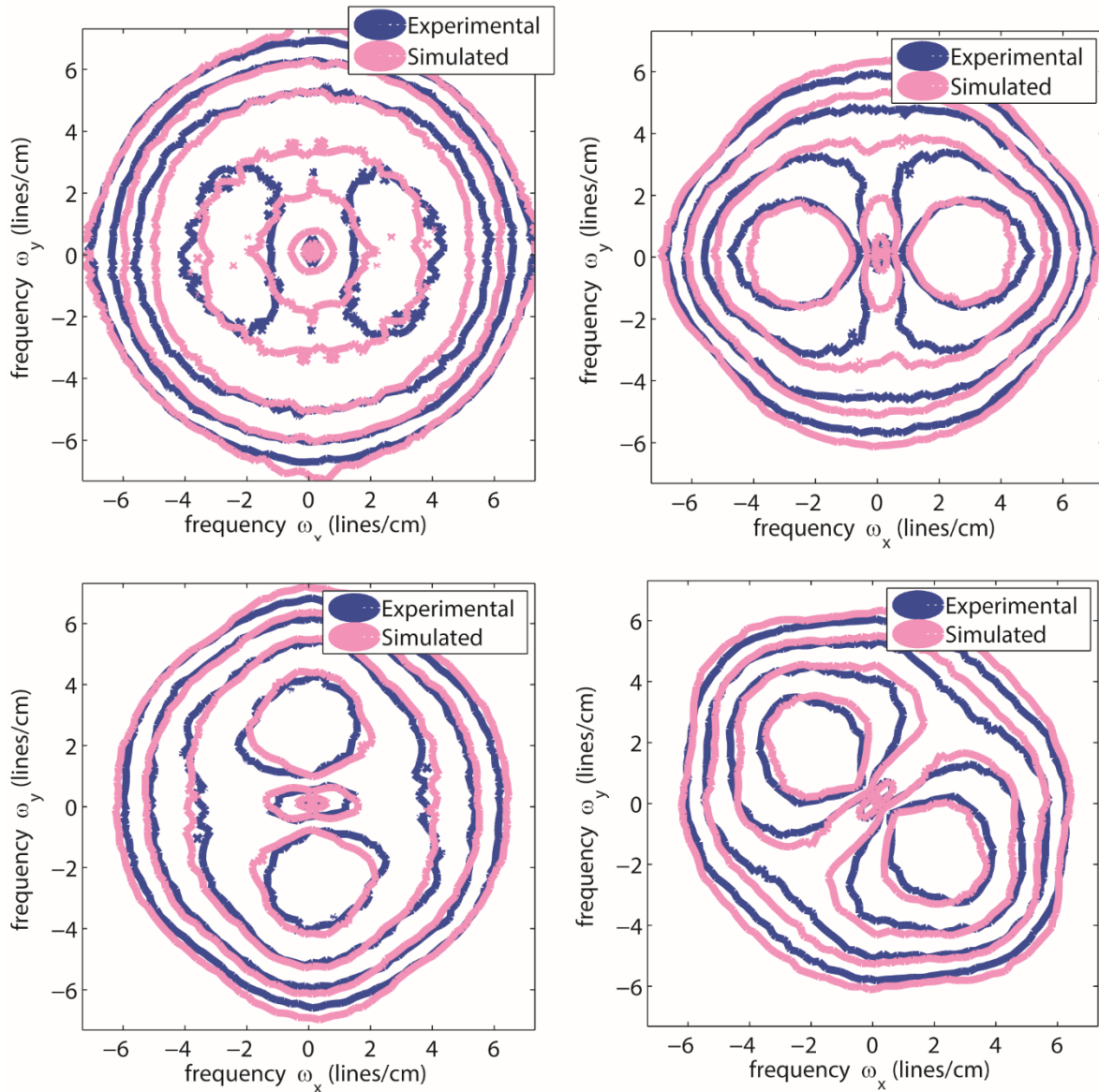
Figure 9: Contour plots of the experimental (blue) and the simulated (pink) NPS at 15 mAs. The iso-contours depict the same value for the pink and blue curves. Each line corresponds to an increase of factor 2 while moving inwards; the actual values for the outermost iso-contours are: 74 Hu^{2}cm^2 (topleft, ROI1), 35 Hu^{2}cm^2 (top right, ROI 2), 35 Hu^{2}cm^2 (left, ROI 3) and 32 Hu^{2}cm^2 (right, ROI 4) These ROI's were indicated in Figure 7.
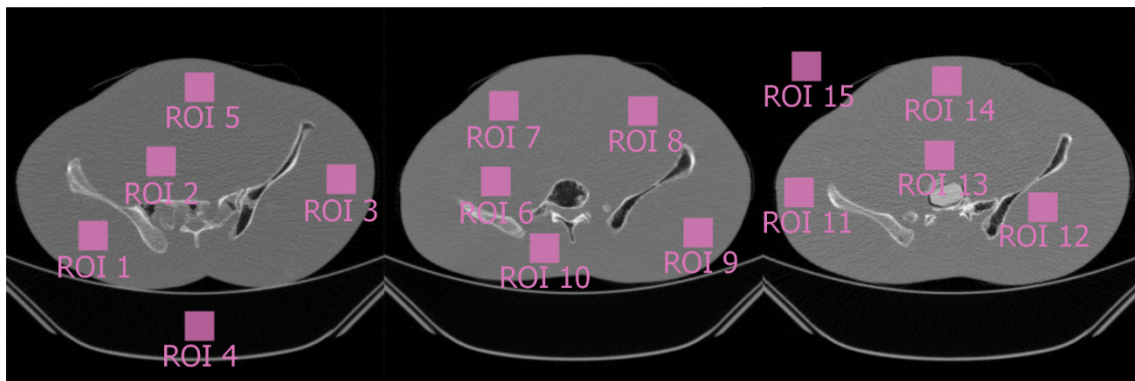
Figure 10: Three slices of the pelvic phantom imaged at 80 mAs in which ROIs were selected for the assessment of the low-dose simulation method.
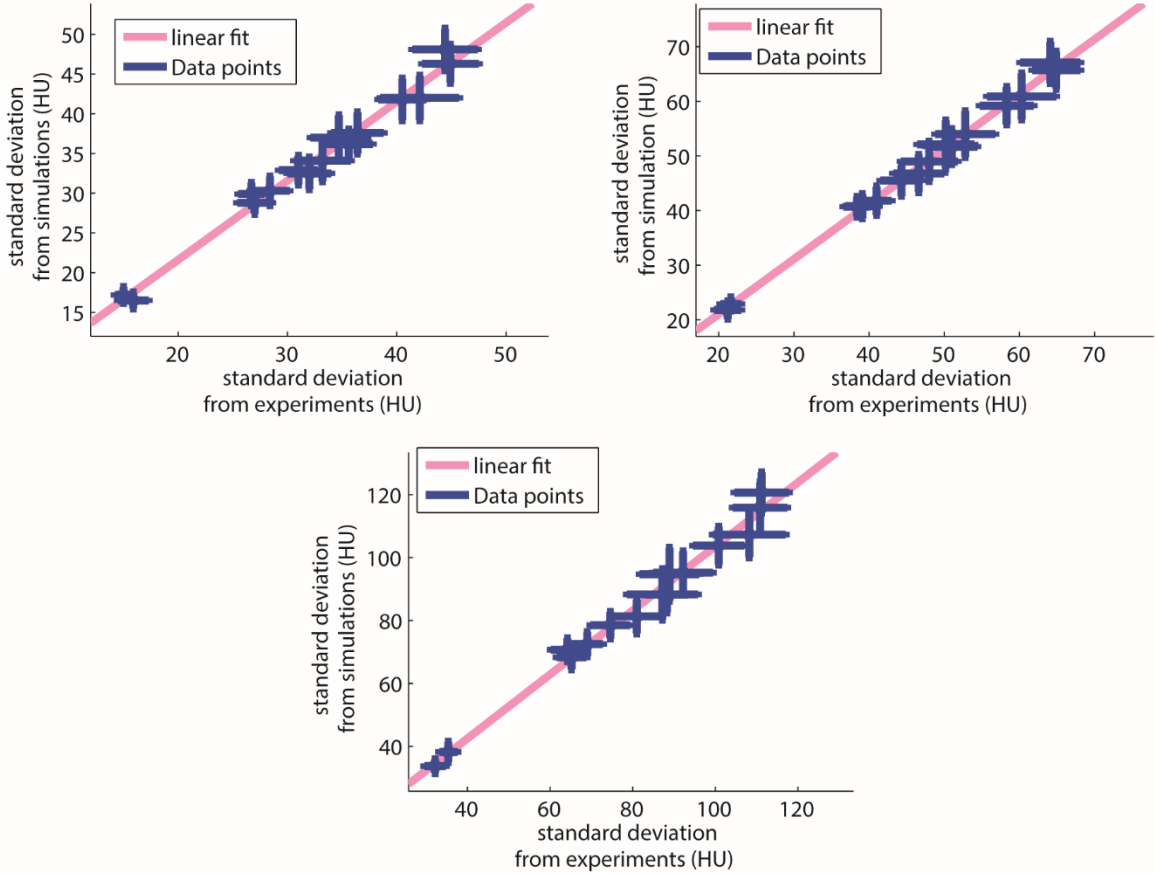

Figure 11: Standard deviations obtained from the simulated images as a function of the ones obtained from the experimentally acquired data at 80 mAs (top left), 40 mAs (top right) and 15 mAs (bottom). Each point indicates the average standard deviation in one of the ROIs depicted in Figure 10. The bars depict the 95% confidence interval of the estimation. The pink line represents the linear fit, the parameters of the fit are listed in Table 3.
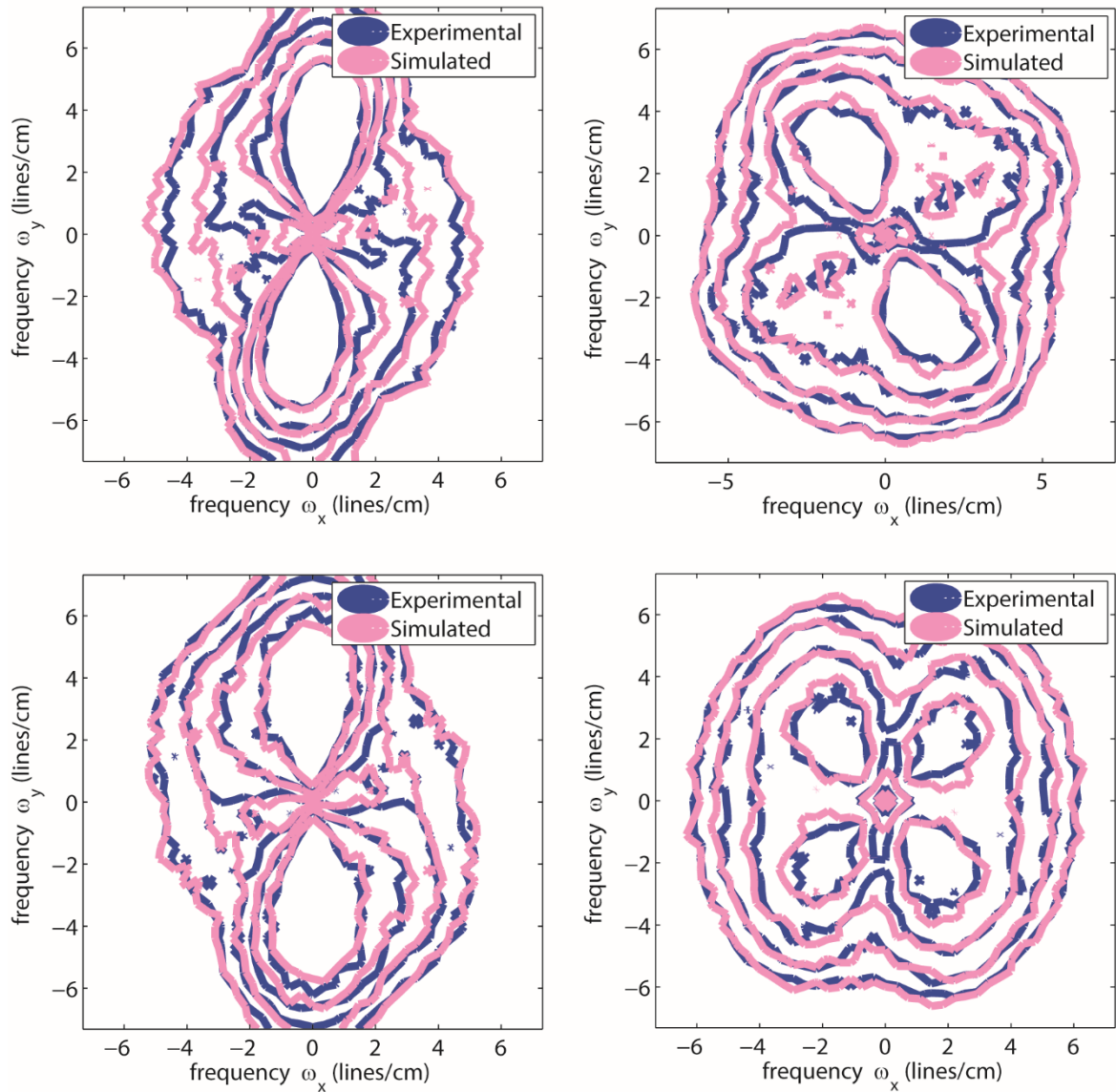
Figure 12: Contour plots of the experimental (blue) and the simulated (pink) NPS from ROIs 3, 7, 12, 14 of the pelvic phantom (depicted in Figure 10) at 15 mAs. The iso-contours depict the same value for the pink and blue curves. Each line corresponds to an increase of factor 2 while moving inwards; the actual values for the outermost iso-contours are: 14 Hu^2cm^2 (top left, ROI 3), 8 Hu^2cm^2 (top right, ROI 7), 18 Hu^2cm^2 (left, ROI 12) and 7 Hu^2cm^2, (right, ROI 14,)

5 Supplementary Material

Appendix A: List of variables

c_{tot}: reconstruction filter coefficients incorporating all the filtering steps

d_{fan}: detector size

H_{tot} : modulation transfer function of the scanner, fourier transform of the reconstruction filter coefficients

H_{filter}: apodized ramp filter

H_{back}: filter representing the interpolation due to backprojection

$H_{fan2par}$: filter representing the interpolation due to resorting the fan-beam projection into parallel-beam geometry

H_{apo}: apodized filter

I: general representation of the tube current

I_{high} : tube current of the high dose image

I_{low} : tube current of the simulated low dose image

I_{red} : tube current of reduced dose image.

i: X-ray beam offset angle with respect to the gantry angle j

j: the gantry angle j

J_{High} : original high dose image in HU

J_{low} : low dose image in HU

J_{noise} : zero-mean noise image in HU

K: X-ray tube output in photons⁄(mAs. mm²)

M: number of gantry angles per rotation

N_0: number of incident photons.

$N_{det,high}$: expected number of detected photons at the exposure level of the high dose image

N_{det} : expected number of detected photons at an arbitrary exposure Iτ

N_{red}: number of photons underlying the reduced-dose measurement

$N_{red,q}$: number of detected photons, drawn from a Poisson distribution

$N_{red,r}$: zero-mean read-out noise signal

N_{fan}: number of detector elements

N_{pix}: number of image pixels

N_l: number of exposure levels

NPS: noise power spectrum

n,m: pixel coordinates

R_{High} : *virtual* high dose sinogram

R_{Noise} : *virtual* zero-mean noise sinogram.

R_{Red} : virtual, 'reduced'-dose sinogram.

T_B: transmission of the bowtie filter

T_{high}: transmission of the object

w: collimation (width of the fan beam)

μ_{High} : attenuation image calculated from the high dose image J_{High}

μ_{Low} : Low dose attenuation image

μ_{noise} : Zero mean noise, attenuation image

μ_{water} : attenuation coefficient of water at the effective energy of an X-ray tube of 80 keV

τ : rotation time

σ_e^2: the variance of the read-out noise

ω_x , ω_y , ω_r: the frequency of image coordinates x,y of radial coordinate r

Appendix B: Scanners geometry parameters

Scanner's geometry parameters	
Number of detector rings	64
Source to isocenter distance, D_{si} (mm)	570
Source to detector distance, D_{sd} (mm)	1040
Field of measurement:D_{FOM} (mm)	500
Number of detectors, N_{det}	672
Detector size, d_{det} (mm)	1.41
Detector size at iso-center, d_{fan} (mm)	~ 0.77
Sampling after rebinning, d_{par} (mm)	$\dfrac{d_{fan}}{2}$
Number of gantry angles per revolution, M	1160

Table 4 Scanner's geometry parameters.

Appendix C: The reconstruction filter

H_{tot} consists of three elements, namely one apodized ramp filter and two interpolation filters. The apodized ramp filter H_{filter} ensures a mathematically correct reconstruction up to the cut-off frequency of the apodization filter. Furthermore, one interpolation filter $H_{fan2par}$ represents the transformation of the fan-beam rays to uniformly sampled parallel-beam rays, and the other one H_{back} reflects the interpolation along the path during the back-projection. Consequently, when aliasing is ignored, H_{tot} is given by:

$$H_{tot}(\omega_r) = H_{filter}(\omega_r) H_{back}(\omega_r) H_{fan2par}(\omega_r),$$ (35)

where H_{filter} is the 'core' backprojection filter, which can be further decomposed into

$$H_{\text{filter}}(\omega_r) = \omega_r H_{\text{apo}}(\omega_r), \tag{36}$$

In which H_{apo} is a cut-off window. The goal is to determine the shape of H_{apo}, which we approximate by:

$$H_{\text{apo}}(\omega_r) = \frac{\left(a + b\cos\left(\dfrac{\pi\omega_r}{f_{par}}\right)\right)}{a+b}, \tag{37}$$

where a and b are two filter parameters. For some values of a and b, $H_{apo}(\omega_r)$ is equal to cut-off windows found in literature [37]. Therefore, Eq. (18) (main text) becomes (after filling in the previous equations):

$$\text{NPS}(\omega_r) = \omega_r \left(\frac{1}{a+b}\right)^2 \left(a + b\cos\left(\frac{\pi\omega_r}{f_{par}}\right)\right)^2 \text{sinc}^4\left(\frac{\omega_r}{f_{fan}}\right)\text{sinc}^4\left(\frac{\omega_r}{f_{par}}\right) \tag{38}$$

in which f_{fan} is the Nyquist frequency of the detector array with detectors of size d_{fan} at the isocenter and f_{par} is the Nyquist frequency of the rebinned detectors of size d_{par}.

Essentially, the parameters a and b are estimated by fitting the model described in Eq. (38) for that we use the Levenberg-Maquardt optimization algorithm.

Appendix D: global comparison between simulated and experimental low-dose scans

The relative root-mean-squared difference between simulated and experimentally measured standard deviation of the noise (ϵ_σ) is an indication of the global performance of our method.

Table 5 and Table 6 show ϵ_σ for varying exposures in the water cylinder and the pelvic phantom, respectively. These tables demonstrate that the simulated noise level closely approximates the experimental noise level in both phantom objects, as ϵ_σ varies from 1-3 %.

Exposure (mAs)	210	170	120	85	60	42	30	21	15
$\epsilon_\sigma(10^{-2})$	1.9	1.4	1.5	1.5	1.4	2.1	2.3	2.3	2.5

Table 5: Relative RMS difference ϵ_σ between simulated and experimentally acquired noise levels as a function of the exposure for all the pixels inside the water cylinder phantom

Exposure (mAs)	80	40	15
$\epsilon_\sigma(10^{-2})$	3.4	3.5	3.1

Table 6: Relative RMS difference ϵ_σ between simulated and experimentally acquired noise levels as a function of the exposure for all pixels inside the pelvic phantom